metals

MDPI

Article

The BCC/B2 Morphologies in $Al_xNiCoFeCr$ High-Entropy Alloys

Yue Ma [1], Beibei Jiang [1], Chunling Li [1], Qing Wang [1,*], Chuang Dong [1], Peter K. Liaw [2], Fen Xu [3] and Lixian Sun [3]

[1] Key Laboratory of Materials Modification by Laser, Ion and Electron Beams (Ministry of Education), School of Materials Science and Engineering, Dalian University of Technology, Dalian 116024, China; mayue@mail.dlut.edu.cn (Y.M.); babywhrs@126.com (B.J.); aianor@163.com (C.L.); dong@dlut.edu.cn (C.D.)

[2] Department of Materials Science and Engineering, The University of Tennessee, Knoxville, TN 37996, USA; pliaw@utk.edu

[3] Guangxi Key Laboratory of Information Materials, Guangxi Collaborative Innovation Center of Structure and Property for New Energy and Materials, School of Material Science and Engineering, Guilin University of Electronic Technology, Guilin 541004, China; xufen@guet.edu.cn (F.X.); sunlx@guet.edu.cn (L.S.)

* Correspondence: wangq@dlut.edu.cn; Tel.: +86-411-84708389

Academic Editors: Michael C. Gao and Junwei Qiao
Received: 31 December 2016; Accepted: 9 February 2017; Published: 15 February 2017

Abstract: The present work primarily investigates the morphological evolution of the body-centered-cubic (BCC)/B2 phases in $Al_xNiCoFeCr$ high-entropy alloys (HEAs) with increasing Al content. It is found that the BCC/B2 coherent morphology is closely related to the lattice misfit between these two phases, which is sensitive to Al. There are two types of microscopic BCC/B2 morphologies in this HEA series: one is the weave-like morphology induced by the spinodal decomposition, and the other is the microstructure of a spherical disordered BCC precipitation on the ordered B2 matrix that appears in HEAs with a much higher Al content. The mechanical properties, including the compressive yielding strength and microhardness of the $Al_xNiCoFeCr$ HEAs, are also discussed in light of the concept of the valence electron concentration (VEC).

Keywords: high-entropy alloys; Al-Ni-Co-Fe-Cr alloys; microstructure; precipitation morphology; mechanical property

1. Introduction

Unlike conventional alloys based on one or two main elements, high-entropy alloys (HEAs) are generally composed of multiple principal elements in equimolar or near-equimolar proportions, also named compositionally-complex alloys (CCAs) [1–6]. This new type of alloys has attracted much attention due to the formation of simple crystalline structures, such as face-centered cubic (FCC)-, body-centered cubic (BCC)-, and close-packed hexagonal (HCP)-solid solutions, as well as their derivatives, instead of complex intermetallic compounds [6–8]. Until now, many HEAs have been reported in diverse systems, e.g., CoCrFeNi-based HEAs [9–14], Al-TMs HEAs (TMs: transition metals) [15–23], and refractory HEAs [24–27]. The special structures render HEAs with the unique performance of excellent mechanical properties and superior corrosion-/oxidation-resistances, as examplified by the fact that the single FCC CoCrFeMnNi HEA shows a remarkably high fracture toughness that outperforms all conventional alloys at cryogenic temperatures [3,6,11].

Typical HEAs were generally formed in Al-containing transition metal (Al-TM) systems, such as $Al_xNiCoFeCr$ [19–22] and $Al_xNiCoFeCrCu$ [15–18], in which the crystalline structures change with the increase of Al content. This variation tendency could also be characterized by the valence electron concentration (VEC) that is closely related to the phase stability [28]. For the $Al_xNiCoFeCr$ HEA series [21], the HEAs with $x \leq 0.45$ (VEC ≥ 7.72) exhibit a single FCC phase, HEAs with $0.45 < x < 0.88$ ($7.30 <$ VEC < 7.72), a dual-phase structure of (FCC + BCC), and those with $x \geq 0.88$ (VEC ≤ 7.30), a single BCC/B2 phase (B2: an ordered BCC phase with a CsCl-type structure). Consequently, the mechanical properties of this series of HEAs would vary with the crystalline structure. The FCC HEAs possess good ductility but lower strength, while the BCC/B2 HEAs have higher strength at the expense of ductility, as demonstrated by the fact that the equimolar AlNiCoFeCr HEA is very brittle with a nearly zero tensile ductility at room temperature due to a weave-like microstructure caused by spinodal decomposition of BCC and B2 phases [19]. However, changing the combination of TMs instead of Al could also make $Al_{0.7}NiCoFe_2Cr$ HEA with a low Al content exhibit a BCC/B2-based structure [29]. More importantly, the unique morphology of the cuboidal B2 phase coherently-embedded into the disordered BCC matrix renders this HEA with both a higher tensile strength (σ_{UTS} = 1223 MPa) and a good ductility of 8% at room temperature. Although the BCC/B2 morphologies were reported in some HEAs sporadically [20,23,30], the elaborate morphology variations of the disordered BCC and its ordered B2 phases have not been studied systematically by far since BCC and B2 phases are always coherent, which is of crucial importance for improving the mechanical property.

Therefore, the present work will aim at the microscopic morphology evolution of the disordered BCC and its ordered B2 phases with increasing the Al content in the $Al_xNiCoFeCr$ HEA series, in which the coherent morphology of the BCC/B2 phases is closely related to the lattice misfit between them. The compressive mechanical property and Vickers hardness of these HEAs will be measured to show the property variation with the microstructure. The present work will contribute to a better understanding of the B2/BCC coherent morphology in HEAs.

2. Experimental Section

The $Al_xNiCoFeCr$ serial alloy ingots were synthesized by arc-melting the raw metal materials under argon atmosphere, in which the purities of raw elemental metals are 99.99% for Al, Co, Fe, Ni, and 99.9% for Cr, respectively. These ingots with a weight of about 15 g were re-melted at least four times to ensure chemical homogeneity, and then copper-mold suction-cast into cylindrical rods with a diameter of 6 mm. The mass loss during the preparation process is less than 0.1%.

The crystalline structures of these suction-cast HEAs were analyzed by a Bruker D8 X-ray diffractometer (XRD, Ettlingen, Germany) with the Cu Kα radiation (λ = 0.15406 nm). The morphologies of HEAs were observed by both Olympus optical microscopy (OM, Tokyo, Japan) and Zeiss Supra55 scanning-electron microscopy (SEM, Oberkochen, Germany) with an etching solution of 5 g $FeCl_3 \cdot 6H_2O$ + 25 mL HCl + 25 mL C_2H_5OH. The further detailed microstructures of HEAs were characterized by the Philips Tecnai G2 transmission-electron microscopy (TEM, Amsterdam, the Netherlands) with a selected-area electron diffraction (SAED) analysis, in which the TEM samples were prepared by twin-jet electro-polishing in a solution of 10% $HClO_4$ + 90% C_2H_5OH (volume fraction) at about −30 °C. The elemental distributions and compositional analyses were measured by the SHIMADZU electron-probe microanalysis (EPMA, Kyoto, Japan). The uniaxial compressive test was performed on an 810 Material Test System (MTS, Cary, NC, USA) with a strain rate of 2×10^{-4} /s at room temperature, in which a strain gage was used for the strain measurement. Two specimens for each alloy were tested with a size of $\phi 3 \times 6$ mm, which were machined from the $\phi 6$ mm alloys rods. Microhardness of HEAs was measured with an HVS-1000 Vickers hardness tester (Laizhou, China) under a load of 500 g for 20 s, in which at least 15 indents were tested to obtain an average value.

3. Experimental Results

3.1. Microstructural Characterization

Alloy compositions in atomic percent (at. %) of this $Al_xNiCoFeCr$ HEA series are listed in Table 1, and all alloys are marked with Al_x hereafter. The XRD results of these suction-cast alloys are shown in Figure 1, from which the $Al_{0.41}$ alloy (S1) with a lower Al content of 9.38 at. % exhibits a single FCC solid solution structure, and the BCC and its ordered B2 phases will appear with increasing the Al content. There exist obvious diffraction peaks of the BCC/B2 phases in the $Al_{0.57}$ alloy (S2, 12.5 at. % Al), although its matrix is still FCC. Then, the BCC and B2 phases are dominant in high-Al HEAs, as demonstrated by the $Al_{0.74}$ alloy (S3, 15.63 at. % Al), and the FCC phase will disappear in the alloys with the Al content larger than 18 at. %, as seen in the XRD patterns of $Al_{0.92}$ (S4), $Al_{1.12}$ (S5), and $Al_{1.33}$ (S6). This trend will be verified further by the OM observations.

Table 1. The alloy compositions, valence electron concentration (VEC), Vickers hardness (HV), compressive mechanical property (yielding strength σ_Y and plasticity δ), and phase constitution of the $Al_xNiCoFeCr$ HEA series.

No.	Alloy Compositions		VEC [1]	HV	σ_Y (MPa)	δ (%)	Phase Constitution
	Molar Proportion	Atomic Percent (at. %)					
S1	$Al_{0.41}NiCoFeCr$ ($Al_{0.41}$)	$Al_{9.38}Ni_{22.66}Co_{22.66}Fe_{22.66}Cr_{22.66}$	7.76	178 ± 7	255	without fracture	FCC matrix + minor BCC
S2	$Al_{0.57}NiCoFeCr$ ($Al_{0.57}$)	$Al_{12.5}Ni_{21.88}Co_{21.88}Fe_{21.88}Cr_{21.88}$	7.59	272 ± 9	607	36	FCC matrix + BCC/B2
S3	$Al_{0.74}NiCoFeCr$ ($Al_{0.74}$)	$Al_{15.63}Ni_{21.09}Co_{21.09}Fe_{21.09}Cr_{21.09}$	7.43	529 ± 11	1394	24	BCC/B2 matrix + minor FCC
S4	$Al_{0.92}NiCoFeCr$ ($Al_{0.92}$)	$Al_{18.75}Ni_{20.31}Co_{20.31}Fe_{20.31}Cr_{20.31}$	7.27	531 ± 9	-	-	BCC/B2
S5	$Al_{1.12}NiCoFeCr$ ($Al_{1.12}$)	$Al_{21.88}Ni_{19.53}Co_{19.53}Fe_{19.53}Cr_{19.53}$	7.10	527 ± 5	1366	17	BCC/B2
S6	$Al_{1.33}NiCoFeCr$ ($Al_{1.33}$)	$Al_{25.00}Ni_{18.75}Co_{18.75}Fe_{18.75}Cr_{18.75}$	6.94	517 ± 7	1348	14	BCC/B2

[1] VEC = Σc_i* $(VEC)_i$.

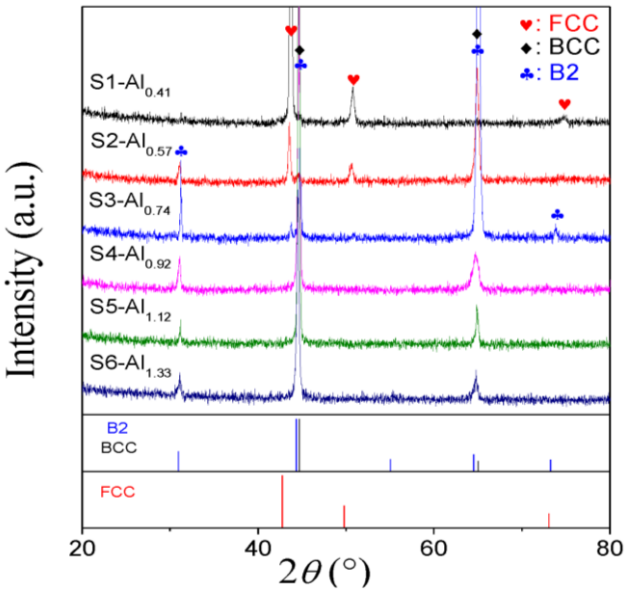

Figure 1. XRD patterns of the suction-cast $Al_xNiCoFeCr$ HEAs.

The main matrix of the $Al_{0.41}$ alloy (S1) shows bright FCC dendrites, as shown in Figure 2a, in which a small amount of BCC/B2 phases is distributed in the inter-dendritic regions (dark region) that could not be detected by XRD. The amount of the inter-dendritic BCC/B2 phases increases with Al, as evidenced by the $Al_{0.57}$ alloy (S2, Figure 2b). In the $Al_{0.74}$ alloy (S3, Figure 2c), the BCC/B2 phases show a microstructure of coarse columnar dendrites, and a minor FCC phase is in the region of inter-dendrites. Further increasing Al to $Al_{1.12}$, the flower-like dendrites are distributed in the matrix (Figure 2e–f), which results from the composition segregation. While in the $Al_{0.92}$ alloy (S4, Figure 2d), the BCC/B2 microstructure exhibits a mixed morphology of major columnar dendrites and minor flower-like ones, in which the latter appears in the central part only (Figure 2d).

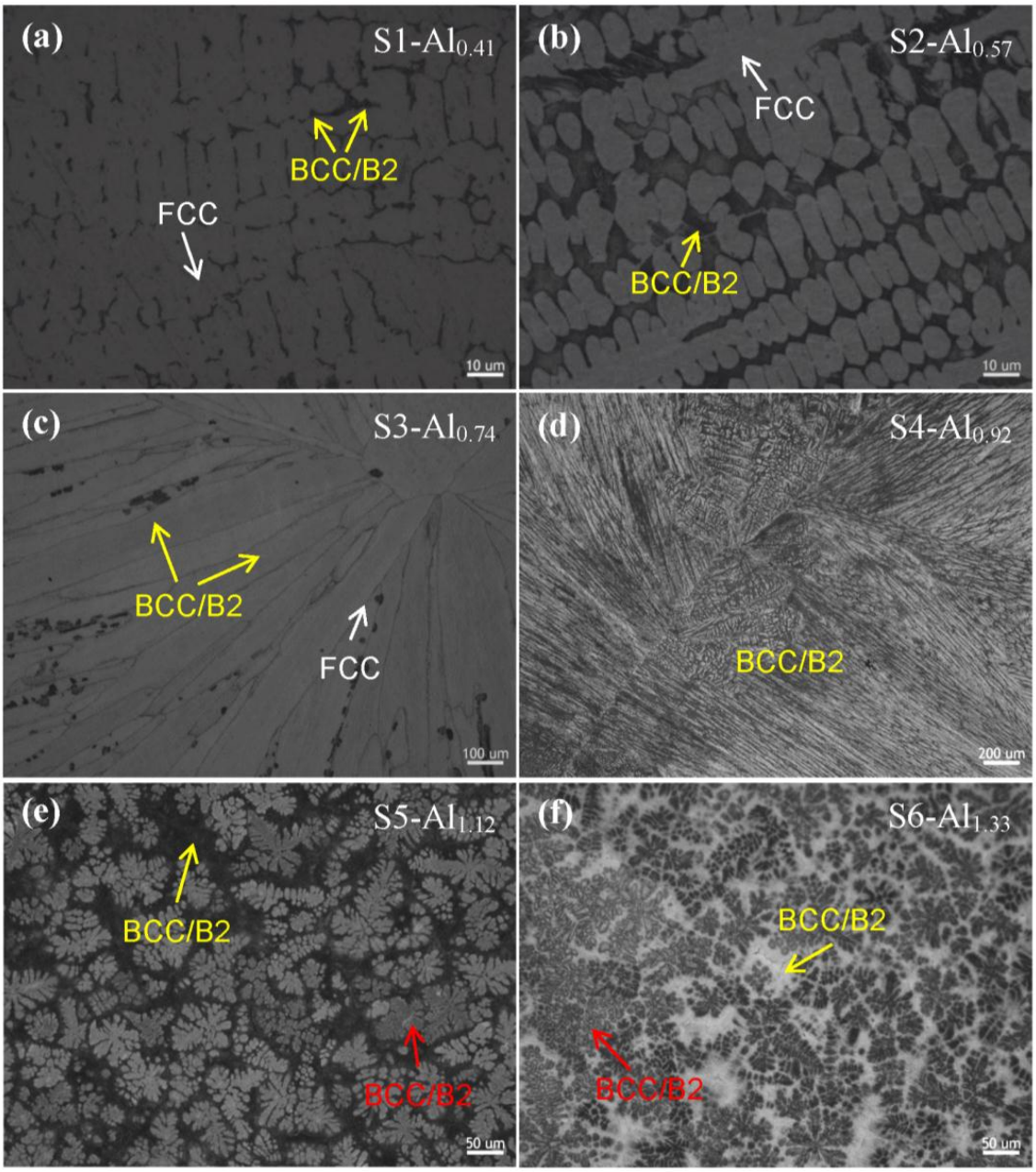

Figure 2. Optical microscopy (OM) graphs of the $Al_xNiCoFeCr$ HEAs. (**a**) S1-$Al_{0.41}$; (**b**) S2-$Al_{0.57}$; (**c**) S3-$Al_{0.74}$; (**d**) S4-$Al_{0.92}$; (**e**) S5-$Al_{1.12}$; (**f**) S6-$Al_{1.33}$.

Figure 3 gives the elemental distributions of the $Al_{1.12}$ alloy (S5) measured by EMPA, from which it could be found that much greater amounts of Al and Ni are aggregated in the flower-like dendrites, and the other inter-dendrites contain much greater contents of Fe and Cr. The measured compositions of the flower-like dendrites and the inter-dendrites are $Al_{26.01}Ni_{23.80}Co_{20.23}Fe_{16.22}Cr_{13.74}$ and $Al_{17.21}Ni_{18.73}Co_{19.77}Fe_{21.70}Cr_{22.59}$ (at. %), respectively, different obviously from the nominal composition of $Al_{21.88}Ni_{19.53}Co_{19.53}Fe_{19.53}Cr_{19.53}$ (at. %). In addition, it is noted that both the flower-like dendrites and the inter-dendrites have BCC and B2 structures without any FCC phase, as evidenced by XRD and the following SEM and TEM studies.

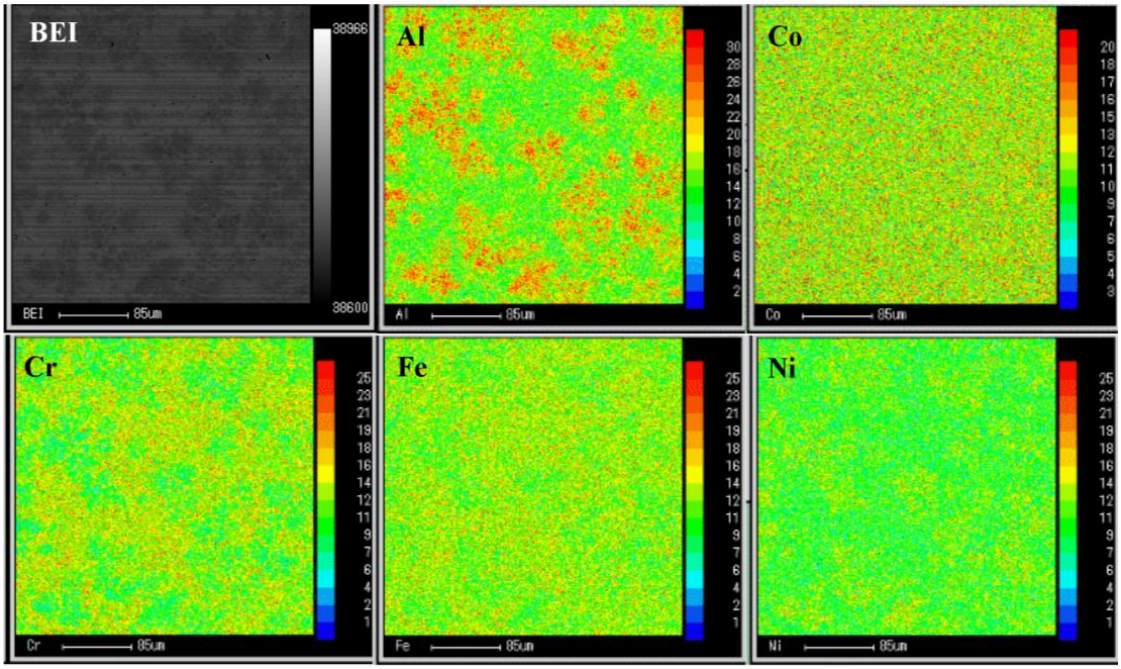

Figure 3. Elemental distributions of the S5-$Al_{1.12}$ HEA mapped by the electron-probe microanalysis (EPMA).

The specific microscopic morphologies of BCC/B2 phases in this HEA series are revealed by highly-magnified SEM images (Figure 4), in which the disordered BCC and its ordered B2 phases always exist coherently. Even in the FCC-based HEAs of $Al_{0.41}$ (S1, Figure 4a) and $Al_{0.57}$ (S2, Figure 4b), the BCC and B2 phases are coherent in the inter-dendrites with a weave-like morphology caused by spinodal decomposition. Such morphology still exists in the BCC $Al_{0.74}$ (S3, Figure 4c) and $Al_{0.92}$ alloys (S4, Figure 4d). When two typical BCC/B2 microstructures induced by composition segregation are obviously different, the microscopic morphologies of BCC/B2 phases would be changed. Take the $Al_{1.12}$ alloy (S5, Figure 4g–i) for instance. In the flower-like dendrites (dark regions in Figure 4g), it is found that spherical nanoparticles are embedded into the matrix (Figure 4i), while the inter-dendrites (bright region in Figure 4g) still show a weave-like morphology (Figure 4h), similar to those in S1–S4 HEAs.

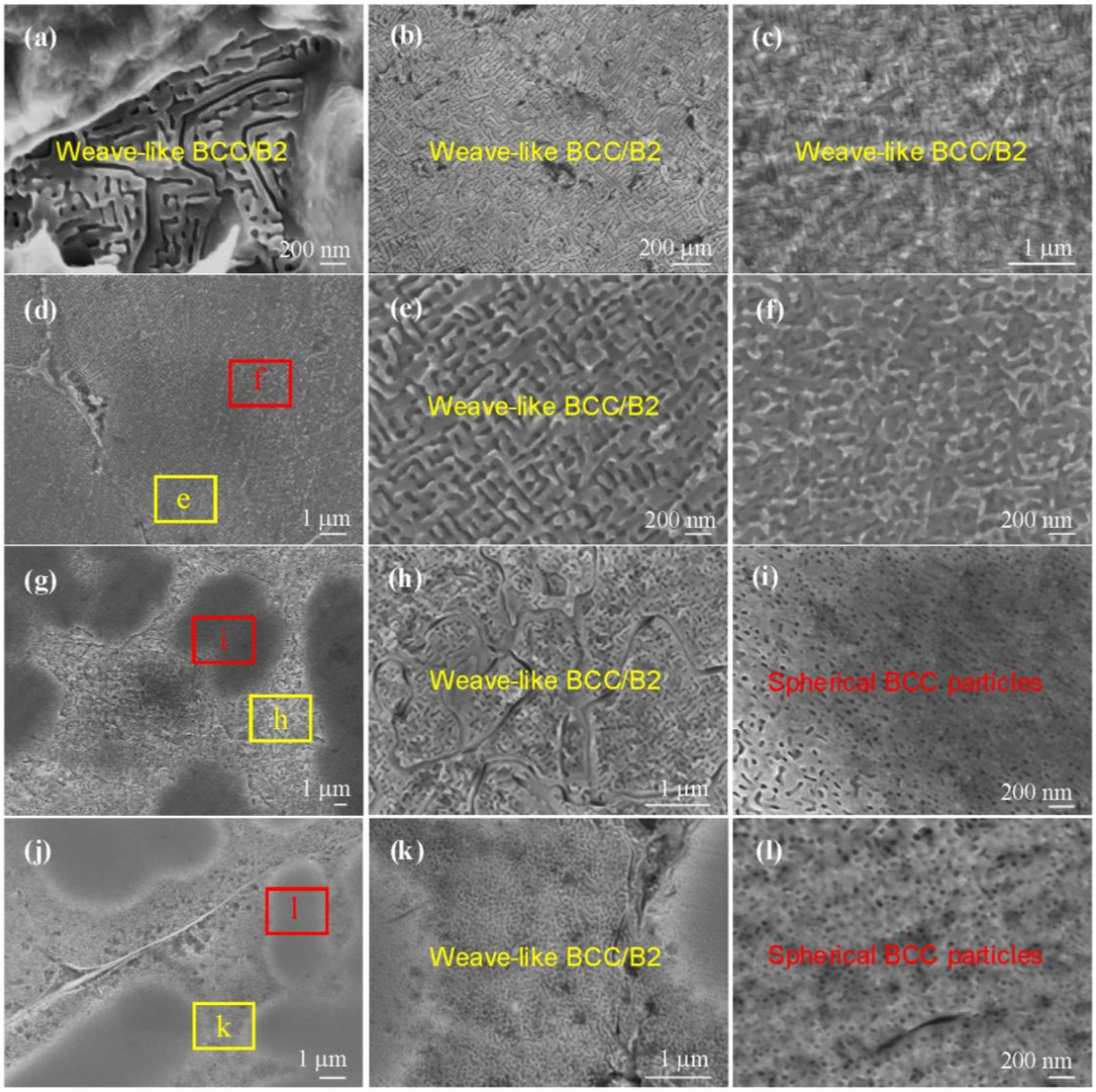

Figure 4. SEM morphologies of the $Al_xNiCoFeCr$ HEAs. (**a**) S1-$Al_{0.41}$; (**b**) S2-$Al_{0.57}$; (**c**) S3-$Al_{0.74}$; (**d**–**f**) S4-$Al_{0.92}$; (**g**–**i**) S5-$Al_{1.12}$; (**j**–**l**) S6-$Al_{1.33}$. Besides the weave-like morphology of BCC and B2 phases, there exists another type of microstructures of spherical BCC nanoparticles distributed in the B2 matrix of high-Al HEAs.

With the further TEM results (Figure 5), the spherical particles with a diameter of about 50 nm are identified as a BCC phase by the dark-field image and SAED pattern (Figure 5b). That is to say, it is the spherical BCC nanoparticles that are coherently precipitated on the ordered B2 matrix in the flower-like dendrites. While the weave-like spinodal decomposition of BCC and B2 phases appears in the inter-dendrites (Figure 5a,c). Similar morphologies of BCC and B2 phases also appear in the $Al_{1.33}$ alloy (S6, Figure 4j–l) with spherical particles in the flower-like dendrites and weave-like spinodal morphology in the other part, in which the size of spherical particles is much smaller, being approximately 20 nm (Figure 5d).

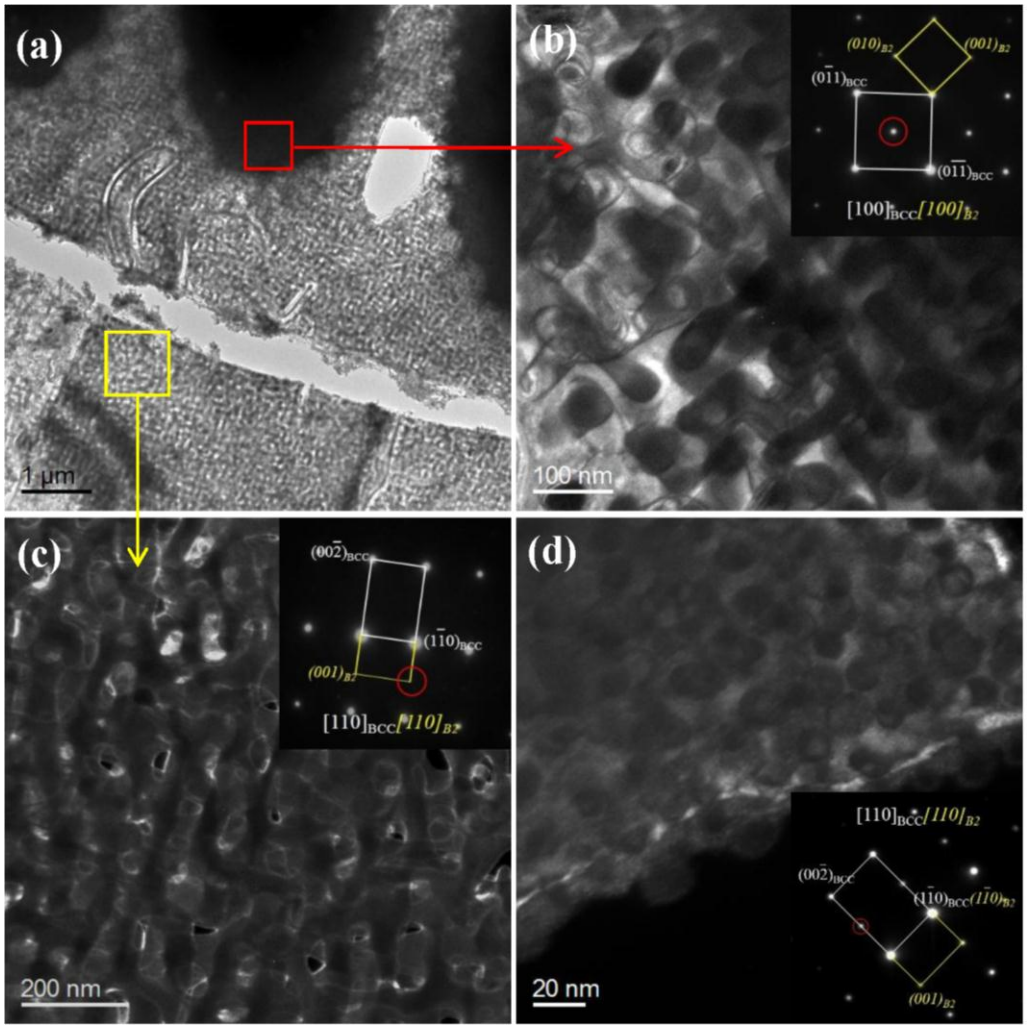

Figure 5. TEM images of the S5-$Al_{1.12}$ (**a**–**c**) and S6-$Al_{1.33}$ (**d**) HEAs. (**a**) is the bright-field image of S5, (**b**) and (**c**) are the magnified dark-field images corresponding to regions in (**a**) marked with the red and yellow rectangles, respectively, showing two types of morphologies of BCC and B2 phases: a morphology of spherical BCC nanoparticles (the SAED pattern in the inset of (**b**)) coherently precipitated in the BCC matrix and a weave-like morphology by spinodal decomposition (**c**). (**d**) is the dark-field image of S6, also showing spherical BCC nanoprecipitates by the SAED pattern in the inset.

3.2. Mechanical Properties

Figure 6 shows engineering compressive stress-strain curves of this $Al_xCoCrFeNi$ HEA series (except the $Al_{0.92}$ alloy (S4)), from which the compressive yielding strength σ_Y and plasticity δ are measured and listed in Table 1. The FCC-based alloy, S1-$Al_{0.41}$, exhibits a good compressive plasticity but a relatively-lower strength with σ_Y = 255 MPa. With the amount of the inter-dendritic BCC/B2 phase increases, the strength is enhanced up to σ_Y = 607 MPa (S2-$Al_{0.57}$). When the BCC/B2 phases are dominant in HEAs, the compressive σ_Y could be enhanced drastically, and keeps constant at a high strength level of 1350–1400 MPa (S3–S6 HEAs). For example, the compressive yielding strength of the $Al_{0.74}$ alloy (S3) is σ_Y = 1394 MPa, much higher than the FCC-based HEAs, even about five times than that of the FCC-based $Al_{0.41}$ alloy. In addition, Table 1 also lists the measured Vickers hardness (HV) of these HEAs, in which the tendency of HV with the crystalline structure is similar than that of the yielding strength.

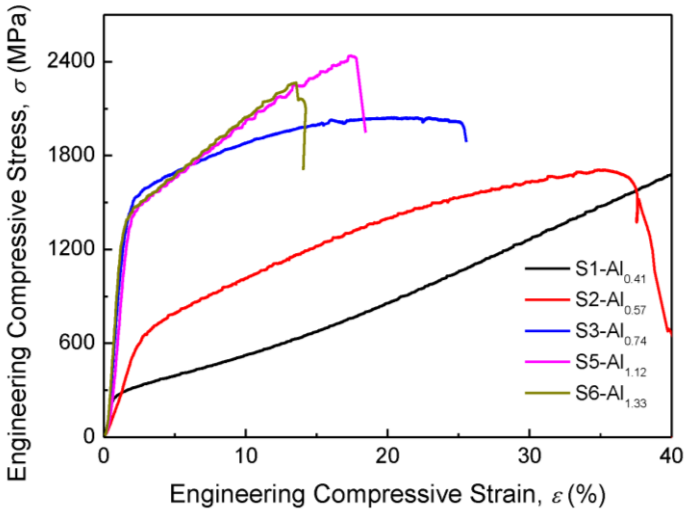

Figure 6. Engineering compressive stress-strain curves of the Al_xNiCoFeCr HEAs.

4. Discussion

4.1. Microscopic Morphologies of BCC/B2 Phases in HEAs

It could be found obviously that whenever the FCC-based HEAs with a low Al content or the BCC/B2 HEAs with a high Al content in the Al_xNiCoFeCr series are present, the ordered B2 phase is always coherent with the disordered BCC phase in the BCC-related regions, as shown in Figures 5 and 6. However, their microscopic morphologies might be different. For instance, in the inter-dendritic regions of the FCC-based $Al_{0.41}$ alloy with a lower Al content of 9.38 at. %, the BCC and B2 phases show a weave-like morphology caused by spinodal decomposition (Figure 4a), which is a typical microstructure in many BCC-based HEAs [20,21]. In the $Al_{1.12}$ alloy (S5) with a high Al content of 21.88 at. %, besides this kind of weave-like morphology, the other kind of morphology of spherical BCC nanoparticles coherently embedded into B2 matrix appears in the flower-like dendrites (Figures 4i and 5b). Such morphology of spherical precipitation of the BCC phase also appears in the $Al_{1.33}$ alloy (S6, Figures 4l and 5d). These two kinds of BCC/B2 microstructures are resulted from the composition segregation, which could be also verified by the XRD results that the diffraction peaks of BCC and B2 phases are widened clearly (Figure 1). Thereof, in the BCC/B2 regions with a very high Al content, the ordered B2 phase becomes the matrix, and the disorder BCC is the precipitated phase with a spherical morphology, which is contrary to the common image that the ordered phase is always precipitated on the disordered BCC matrix [30–36].

It is known that the size and the shape of precipitates are crucial for the mechanical properties of conventional alloys. Especially if the shape of the precipitates is closely related to the lattice misfit, ε, between the precipitated phase and the matrix phase [29,31–38]. Generally speaking, a smaller lattice misfit, ε, leads to a spherical shape, and when the misfit becomes larger, it is difficult to control the morphology of the precipitates, and the coherency between them will disappear gradually, resulting in coarse second particles finally. Only a moderate ε, neither large nor small, can produce cuboidal coherent precipitates, leading to excellent mechanical properties. Such a case is common in Ni-based superalloys [33,34], in which the cuboidal ordered nanoparticles with a $L1_2$ structure (Ni_3Al-type) are coherently embedded into the disordered FCC matrix, exhibiting an incomparable mechanical property at high temperatures. While in sharp contrast, the weave-like spinodal morphology of ordered and disordered coherent phases with a relatively-larger ε will deteriorate alloy properties, as exemplified by the brittle AlNiCoFeCr HEA [19].

Thus, the lattice misfit between the disordered BCC and the ordered B2 phases in this present HEA series are calculated with the formula of $\varepsilon = 2 \times (\alpha_{B2} - \alpha_{BCC})/(\alpha_{B2} + \alpha_{BCC})$, where α_{B2} and α_{BCC}

are the lattice constants of B2 and BCC phases, respectively. Here, the lattice constants of BCC and B2 phases in $Al_{0.57}$ (S2), $Al_{0.74}$ (S3), and $Al_{0.92}$ (S4) HEAs were calculated from XRD, and those in $Al_{1.12}$ (S5) and $Al_{1.33}$ (S6) HEAs were achieved from TEM. Table 2 lists these lattice constants (α_{B2} and α_{BCC}), lattice misfits ε, and their corresponding microscopic morphologies of BCC and B2 phases. It could be concluded that a larger absolute value of ε ($\varepsilon > 0.53\%$) corresponds to a weave-like morphology caused by the spinodal decomposition of BCC and B2 phases. A smaller ε ($\varepsilon < 0.10\%$) can produce another morphology of spherical particles coherently precipitated into the matrix. Only a moderate ε can produce cuboidal precipitates, as demonstrated by the fact that the cuboidal B2 nanoprecipitates are coherently embedded into the BCC matrix in the BCC $Al_{0.57}NiCoFe_2Cr$ HEA with a $\varepsilon = -0.38\%$ [29].

Table 2. The lattice misfits ε and the corresponding morphologies of BCC and B2 phases in the $Al_xNiCoFeCr$ HEAs, in which the lattice constants (α_{B2} and α_{BCC}) of BCC and B2 phases calculated from both XRD and TEM analysis are also included.

No.	α_{B2} (Å)	α_{BCC} (Å)	ε [1] (%)	Morphology
S2-$Al_{0.57}$	2.871	2.854	0.59	Weave-like spinodal decomposition
S3-$Al_{0.74}$	2.855	2.870	−0.53	Weave-like
S4-$Al_{0.92}$	2.878	2.897	−0.69	Weave-like
S5-$Al_{1.12}$	2.809	2.831	−0.78	Weave-like
	2.855	2.858	−0.11	Spherical particles
S6-$Al_{1.33}$	2.908	2.911	−0.10	Spherical particles
$Al_{0.7}NiCoFe_2Cr$ [29]	2.851	2.862	−0.38	Cuboidal particles

[1] $\varepsilon = 2 \times (\alpha_{B2} - \alpha_{BCC})/(\alpha_{B2} + \alpha_{BCC})$.

In fact, the weave-like morphology of BCC and B2 phases is common in the Al-containing BCC HEAs, which is due to that Al affects the lattice constants of BCC and B2 strongly, leading to a large lattice misfit ε. Moreover, the ε could increase with the Al content, as a result of a serious spinodal decomposition. Similar to Al, the elements Ti and Zr also can produce a larger misfit, as exemplified by the fact that the lattice misfit of $\varepsilon = 2.38\%$ between BCC and B2 phases in the refractory $Al_{0.3}NbTaTi_{1.4}Zr_{1.3}$ BCC HEA is so high that a consequent spinodal decomposition seriously deteriorates the plasticity [24]. Thereof, it is difficult to obtain a moderate lattice misfit of BCC and B2 phases for an expected morphology through tuning Al (Ti, Zr) in BCC-based HEAs since they obviously affect the lattice constants.

4.2. Relationship among σ_Y, HV, and Structure with VEC of HEAs

It is well known that the phase stability of an alloy is related to multiple factors simultaneously, such as the atom size, electron concentration, and enthalpy of mixing [39–42]. Here the valence electron concentration (VEC) is introduced to characterize the strength evolution of the designed HEAs due to its simplicity. It can be calculated with the formula of $VEC = \Sigma c_i \times (VEC)_i$, where c_i is the atomic percentage and $(VEC)_i$ is the VEC value for the i element, being 3 for Al, 6 for Cr, 8 for Fe, 9 for Co, and 10 for Ni, respectively. Figure 7 shows the compressive yielding strength, σ_Y, and Vickers hardness, HV, as a function of VEC of this HEA series, in which the VEC for the characterization of the BCC/B2 region is VEC < 7.4. The σ_Y and HV of HEAs with a dual-phase of BCC and FCC HEAs would be obviously enhanced by increasing the amount of the BCC/B2 phases. While the σ_Y and HV of the BCC HEAs keep almost constant at a relatively-higher strength level (σ_Y = 1350–1400 MPa, HV = 520–530) at the expense of plasticity with decreasing VEC (Table 1). In comparison with the BCC-based $Al_{0.7}NiCoFe_2Cr$ HEA ($Al_{12.5}Ni_{17.5}Co_{17.5}Fe_{35.0}Cr_{17.5}$ at. %, VEC = 7.55) with cuboidal B2 nanoprecipitates coherent with the BCC matrix [28], exhibiting a compressive strength of σ_Y = 1166 MPa (HV = 486) and a plasticity of δ = 30.2%, the $Al_{0.74}$ alloy (S2) with the same Al content exhibits a FCC matrix with a relatively-lower strength (σ_Y = 607 MPa). While the plasticity of this BCC $Al_xNiCoFeCr$ series with high Al contents are

decreased obviously although they have a higher strength (Table 1 and Figure 6). Therefore, changing the combination of transition metals to substitute for the Al could achieve a moderate lattice misfit for the cuboidal morphology of B2 precipitates in the BCC matrix, which renders the HEAs with high strength and good ductility.

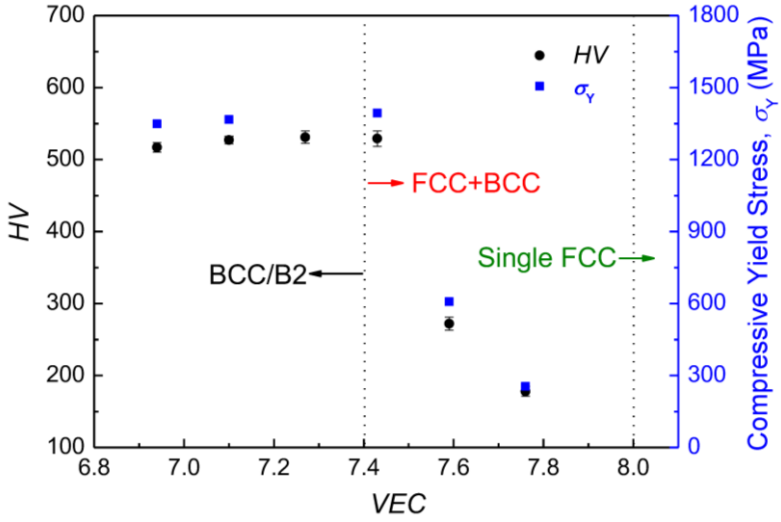

Figure 7. The tendencies of compressive yielding stress, σ_Y, and microhardness, HV, with VEC of the Al_xNiCoFeCr HEAs.

5. Conclusions

The evolutions of microstructures and mechanical properties of the Al_xNiCoFeCr HEA series with the changing Al content have been studied, in which the microscopic morphologies of disordered BCC and ordered B2 phases were investigated particularly. It is found that the B2 phase is always coherently present with the BCC phase in the BCC-related regions of both FCC-based and BCC HEAs. There are two typical morphologies of BCC/B2 phases in this alloy series, one being the weave-like spinodal morphology and the other the morphology of spherical BCC nanoprecipitates in the B2 matrix. The shapes of coherent precipitates are closely related to the absolute value of the lattice misfit, ε, between BCC and B2 phases, in which a small ε ($\varepsilon < 0.10\%$) could produce a spherical precipitation and a larger ε ($\varepsilon > 0.53\%$) corresponds to a weave-like spinodal decomposition that is sensitive to Al. The Al_xNiCoFeCr BCC HEAs possess a higher strength (compressive σ_Y = 1350–1400 MPa) at the expense of plasticity. That tuning the combination of transition metals instead of Al is expected to obtain a moderate ε for cuboidal precipitation, which will lead to prominent mechanical properties.

Acknowledgments: This work was supported by the National Natural Science Foundation of China (No. 51171035), the International Science & Technology Cooperation Program of China (No. 2015DFR60370), the Natural Science Foundation of Liaoning Province of China (No. 2015020202), the Foundation of Guangxi Key Laboratory of Information Materials [No. 161002-K], and the Fundamental Research Funds for the Central Universities (No. DUT16ZD212). P.K. Liaw would like to acknowledge the Department of Energy (DOE), Office of Fossil Energy, National Energy Technology Laboratory (DE-FE-0008855, DE-FE-0024054, and DE-FE-0011194), the U.S. Army Research Office project (W911NF-13-1-0438), the National Science Foundation (DMR-1611180), and the QuesTek Innovations LLC (No. DE-SC0013220).

Author Contributions: Qing Wang conceived and designed the experiments; Yue Ma performed the experiments, analyzed the data, and wrote the paper; Beibei Jiang and Chunling Li provided assistance in the experiments; Chuang Dong and Peter K. Liaw discussed the results and modified the paper; Fen Xu and Lixian Sun contributed reagents/materials.

Conflicts of Interest: The authors declare no conflicts of interest.

References

1. Miracle, D.B.; Senkov, O.N. A critical review of high entropy alloys and related concepts. *Acta Mater.* **2016**, *122*, 488–511. [CrossRef]
2. Senkov, O.N.; Miller, J.D.; Miracle, D.B.; Woodward, C. Accelerated exploration of multi-principal element alloys with solid solution phases. *Nature Commun.* **2015**, *6*, 7529. [CrossRef] [PubMed]
3. Zhang, Y.; Zuo, T.T.; Tang, Z.; Gao, M.C.; Dahmen, K.A.; Liaw, P.K.; Lu, Z.P. Microstructures and properties of high-entropy alloys. *Prog. Mater. Sci.* **2014**, *61*, 1–93. [CrossRef]
4. Ye, Y.F.; Wang, Q.; Lu, J.; Liu, C.T.; Yang, Y. High-entropy alloy: Challenges and prospects. *Mater. Today* **2016**, *19*, 349–362. [CrossRef]
5. Yeh, J.W.; Chen, S.K.; Lin, S.J.; Gan, J.Y.; Chin, T.S.; Shun, T.T.; Tsau, C.H.; Chang, S.Y. Nanostructured high-entropy alloys with multiple principal elements: Novel alloy design concepts and outcomes. *Adv. Eng. Mater.* **2004**, *6*, 299–303. [CrossRef]
6. Diao, H.; Xie, X.; Sun, F.; Dahmen, K.A.; Liaw, P.K. Mechanical properties of high-entropy alloys. In *High-Entropy Alloys: Fundamentals and Applications*; Gao, M.C., Yeh, J.W., Liaw, P.K., Zhang, Y., Eds.; Springer International Publishing: Gewerbestrasse, Switzerland, 2016; pp. 181–236.
7. Zhang, Y.; Zhou, Y.J.; Lin, J.P.; Chen, G.; Liaw, P.K. Solid-solution phase formation rules for multi-component alloys. *Adv. Eng. Mater.* **2008**, *10*, 534–538. [CrossRef]
8. Youssef, K.M.; Zaddach, A.J.; Niu, C.; Irving, D.L.; Koch, C.C. A novel low-density, high-hardness, high-entropy alloy with close-packed Single-phase Nanocrystalline Structures. *Mater. Res. Lett.* **2014**, *2*, 95–99. [CrossRef]
9. Schuh, B.; Mendez-Martin, F.; Volker, B.; George, E.P.; Clemens, H.; Pippan, R.; Hohenwarter, A. Mechanical properties, microstructure and thermal stability of a nanocrystalline CoCrFeMnNi high-entropy alloy after severe plastic deformation. *Acta Mater.* **2015**, *96*, 258–268. [CrossRef]
10. Salishchev, G.A.; Tikhonovsky, M.A.; Shaysultanov, D.G.; Stepanov, N.D.; Kuznetsov, A.V.; Kolodiy, I.V.; Tortika, A.S.; Senkov, O.N. Effect of Mn and V on structure and mechanical properties of high-entropy alloys based on CoCrFeNi system. *J. Alloy. Compd.* **2014**, *591*, 11–21. [CrossRef]
11. Gludovatz, B.; Hohenwarter, A.; Catoor, D.; Chang, E.H.; George, E.P.; Ritchie, R.O. A fracture-resistant high-entropy alloy for cryogenic applications. *Science* **2014**, *345*, 1153–1158. [CrossRef] [PubMed]
12. Tsai, K.Y.; Tsai, M.H.; Yeh, J.W. Sluggish diffusion in Co–Cr–Fe–Mn–Ni high-entropy alloys. *Acta Mater.* **2013**, *61*, 4887–4897. [CrossRef]
13. Owen, L.R.; Pickering, E.J.; Playford, H.Y.; Stone, H.J.; Yucker, M.G.; Jones, N.G. An assessment of the lattice strain in the CrMnFeCoNi high-entropy alloy. *Acta Mater.* **2017**, *122*, 11–18. [CrossRef]
14. Otto, F.; Dlouhy, A.; Somsen, C.; Bei, H.; Eggeler, G.; George, E.P. The influences of temperature and microstructure on the tensile properties of a CoCrFeMnNi high-entropy alloy. *Acta Mater.* **2013**, *61*, 5743–5755. [CrossRef]
15. Singh, S.; Wanderka, N.; Murty, B.S.; Glatzel, U.; Banhart, J. Decomposition in multi-component AlCoCrCuFeNi high-entropy alloy. *Acta Mater.* **2011**, *59*, 182–190. [CrossRef]
16. Kuznetsova, A.V.; Shaysultanov, D.G.; Stepanov, N.D.; Salishchev, G.A.; Senkov, O.N. Tensile properties of an AlCrCuNiFeCo high-entropy alloy in as-cast and wrought conditions. *Mater. Sci. Eng. A* **2012**, *533*, 107–118. [CrossRef]
17. Hemphill, M.A.; Yuan, T.; Wang, G.Y.; Yeh, J.W.; Tsai, C.W.; Chuang, A.; Liaw, P.K. Fatigue behavior of Fatigue behavior of $Al_{0.5}$CoCrCuFeNi high entropy alloys high entropy alloys. *Acta Mater.* **2012**, *60*, 5723–5734. [CrossRef]
18. Pickering, E.J.; Stone, H.J.; Jones, N.G. Fine-scale precipitation in the high-entropy alloy $Al_{0.5}$CrFeCoNiCu. *Mater. Sci. Eng. A* **2015**, *645*, 65–71. [CrossRef]
19. Wang, W.R.; Wang, W.L.; Yeh, J.W. Phases, microstructure and mechanical properties of Al_xCoCrFeNi high-entropy alloys at elevated temperatures. *J. Alloy. Compd.* **2014**, *589*, 143–152. [CrossRef]
20. Wang, W.R.; Wang, W.L.; Wang, S.C.; Tsai, Y.C.; Lai, C.H.; Yeh, J.W. Effects of Al addition on the microstructure and mechanical property of Al_xCoCrFeNi high-entropy alloys. *Intermetallics* **2012**, *26*, 44–51. [CrossRef]
21. Kao, Y.F.; Chen, T.J.; Chen, S.K.; Yeh, J.W. Microstructure and mechanical property of as-cast, -homogenized, and -deformed Al_xCoCrFeNi ($0 \leq x \leq 2$) high-entropy alloys. *J. Alloy. Compd.* **2009**, *488*, 57–64. [CrossRef]

22. Li, D.; Li, C.; Feng, T.; Zhang, Y.; Sha, G.; Lewandowski, J.J.; Liaw, P.K.; Zhang, Y. High-entropy $Al_{0.3}$CoCrFeNi alloy fibers with high tensile strength and ductility at ambient and cryogenic temperature. *Acta Mater.* **2017**, *123*, 285–294. [CrossRef]
23. Choudhuri, D.; Gwalani, B.; Gorsse, S.; Mikler, C.V.; Ramanujan, R.V.; Gibson, M.A.; Banerjee, R. Change in the primary solidification phase from fcc to bcc -based B2 in high entropy or complex concentrated alloys. *Scr. Mater.* **2017**, *127*, 186–190. [CrossRef]
24. Senkov, O.N.; Woodward, C.; Miracle, D.B. Microstructure and properties of aluminum-containing refractory high-entropy alloys. *JOM* **2014**, *66*, 2030–2042. [CrossRef]
25. Senkov, O.N.; Senkova, S.V.; Woodward, C. Effect of aluminum on the microstructure and properties of two refractory high-entropy alloys. *Acta Mater.* **2014**, *68*, 214–228. [CrossRef]
26. Qiu, Y.; Hu, Y.J.; Taylor, A.; Styles, M.J.; Marceau, R.K.W.; Ceguerra, A.V. A lightweight single-phase AlTiVCr compositionally complex alloy. *Acta Mater.* **2017**, *123*, 115–124. [CrossRef]
27. Senkov, O.N.; Wilks, G.B.; Miracle, D.B.; Chuang, C.P.; Liaw, P.K. Refractory high-entropy alloys. *Intermetallics* **2010**, *18*, 1758–1765. [CrossRef]
28. Guo, S.; Ng, C.; Lu, J.; Liu, C.T. Effect of valence electron concentration on stability of FCC or BCC phase in high entropy alloys. *J. Appl. Phys.* **2011**, *109*, 645–647. [CrossRef]
29. Wang, Q.; Ma, Y.; Jiang, B.B.; Li, X.; Shi, Y.; Dong, C.; Liaw, P.K. A cuboidal B2 nanoprecipitation-enhanced body-centered-cubic alloy $Al_{0.7}CoCrFe_2Ni$ with prominent tensile properties. *Scr. Mater.* **2016**, *120*, 85–89. [CrossRef]
30. Niu, S.; Kou, H.; Guo, T.; Zhang, Y.; Wang, J.; Li, J. Strengthening of nanoprecipitations in an annealed $Al_{0.5}$CoCrFeNi high entropy alloy. *Mater. Sci. Eng. A* **2016**, *671*, 82–86. [CrossRef]
31. He, J.Y.; Wang, H.; Huang, H.L.; Xu, X.D.; Chen, M.W.; Wu, Y.; Liu, X.J.; Nieh, T.G. A precipitation-hardened high-entropy alloy with outstanding tensile properties. *Acta Mater.* **2016**, *102*, 187–196. [CrossRef]
32. Ma, K.K.; Wen, H.; Hu, T.; Topping, T.D.; Isheim, D.; Seidman, D.N.; Lavernia, E.J.; Schoenung, J.M. Mechanical behavior and strengthening mechanisms in ultrafine grain precipitation-strengthened aluminum alloy. *Acta Mater.* **2014**, *61*, 141–155. [CrossRef]
33. Reed, R.C. *The Superalloys: Fundamentals and Applications*; Cambridge University Press: New York, NY, USA, 2006; pp. 152–157.
34. Wang, X.G.; Liu, J.L.; Jin, T.; Sun, X.F. The effects of ruthenium additions on tensile deformation mechanisms of single crystal superalloys at different temperatures. *Mater. Des.* **2014**, *63*, 286–293. [CrossRef]
35. Sato, J.; Omori, T.; Oikawa, K.; Ohnuma, I.; Kainuma, R.; Ishida, K. Cobalt-base high-temperature alloys. *Science* **2006**, *312*, 90–91. [CrossRef] [PubMed]
36. Teng, Z.K.; Miller, M.K.; Ghosh, G.; Liu, C.T.; Huang, S.; Russell, K.F.; Fine, M.E.; Liaw, P.K. Characterization of nanoscale NiAl-type precipitates in a ferritic steel by electron microscopy and atom probe tomography. *Scr. Mater.* **2010**, *63*, 61–64. [CrossRef]
37. Jensen, J.K.; Welk, B.A.; Williams, R.E.A.; Sosa, J.M.; Huber, D.E.; Senkov, O.N.; Viswanathan, G.B.; Fraser, H.L. Characterization of the microstructure of the compositionally complex alloy $Al_1Mo_{0.5}Nb_1Ta_{0.5}Ti_1Zr_1$. *Scr. Mater.* **2016**, *121*, 1–4. [CrossRef]
38. Senkov, O.; Isheim, D.; Seidman, D.N.; Pilchak, A.L. Development of a refractory high entropy superalloy. *Entropy* **2016**, *18*, 102. [CrossRef]
39. Mizutani, U. The Hume-Rothery rules for structurally complex alloy phases. *MRS Bull.* **2012**, *37*, 2515–2525. [CrossRef]
40. Hume-Rothery, W.; Smallman, R.E.; Haworth, C.W. *The Structure of Metals and Alloys*; The Institute of Metals: London, UK, 1969.
41. Egami, T.; Waseda, Y. Atomic size effect on the formability of metallic glasses. *J. Non-Cryst. Solids* **1984**, *64*, 113–134. [CrossRef]
42. Yang, X.; Zhang, Y. Prediction of high-entropy stabilized solid-solution in multi-component alloys. *Mater. Chem. Phys.* **2012**, *132*, 233–238. [CrossRef]